Piecewise Smoothed Value Picking Regularization Applied to 2-D TM and TE Inverse Scattering

Sara Van den Bulcke, Ann Franchois, *Senior Member, IEEE*, and Daniël De Zutter, *Fellow, IEEE*

***Abstract*—The Stepwise Relaxed Value Picking (SRVP) regularization technique, proposed earlier for the iterative reconstruction of piecewise (quasi-)homogeneous objects, is a non-spatial technique, whereby the reconstruction unknowns are clustered around a limited number of—*a-priori* unknown—reference values. Artifacts have been observed in some 2-D and 3D complex permittivity reconstructions. This paper therefore combines the non-spatial SRVP technique with a spatial smoothing technique, whereby the reference values provided by the former—in each iteration—are employed by the latter to define separate smoothing regions. This way edges are preserved, since the spatial smoothing constraints in the cost function are active within but not across the region boundaries. This combined technique, denoted as Stepwise Relaxed Piecewise Smoothed Value Picking (SRPSVP) regularization, is formulated for the 2.5D microwave inverse scattering problem and is illustrated with reconstructions from the Institut Fresnel 2-D scattering database.**

***Index Terms*—Complex permittivity, inverse scattering, microwave imaging, optimization, piecewise smoothing, reconstruction, regularization.**

I. Introduction

REGULARIZATION by imposing spatial smoothing constraints on the entire reconstructed profile as in [1]–[3] is less suitable for piecewise homogeneous objects. Imaging piecewise homogeneous objects is of interest in various applications in non-destructive testing [4] and subsurface sensing [5]. Several spatial smoothing techniques have been proposed to enhance edges in nonlinear inverse scattering algorithms, e.g., L1-norm total variation (TV) regularization [6], edge-preserving regularization [7] with weighted L2-norm TV [8] and with various potential functions [9], [10]. Other methods are dedicated specifically to piecewise homogeneous profiles, e.g., the level-set algorithm for binary or n-ary objects [11], [12]. Stepwise Relaxed Value Picking (SRVP) regularization [13] was proposed for piecewise (quasi-)homogeneous objects and has yielded promising results for the inversion of the three-dimensional (3D) [14] and 2-D [15] microwave scattering databases from Institut Fresnel and for 2.5D millimeter-wave imaging of concealed objects [16].

Value Picking (VP) regularization is a non-spatial technique—it does not operate on the spatial neighborhood of the reconstruction variable—which gradually clusters the reconstruction unknowns around a limited number of *a-priori* unknown reference values—the VP values—which in turn are adjusted during the iterative reconstruction process by means of a well-chosen regularizing function. The regularization thus encourages each reconstruction variable to converge towards one of these VP values. The basic idea of enforcing piecewise homogeneity by introducing reference values in the cost function has been explored for binary objects in [17], [18] and for one extra permittivity value in [19], but the choice function in those previous works differs from the one used in the VP regularization technique. The VP choice function is defined for any number of permittivities and has well-documented properties [13]; in particular it is "less than quadratic", hence it easily can be incorporated in the Gauss-Newton algorithm through a sequence of quadratic approximations. The Stepwise Relaxed (SR) approach refers to applying a severe regularization in the beginning of the iterations, by using only one VP value—the complex permittivity of the background—and gradually relaxing the regularization by adding new VP values. This considerably improves the convergence of the algorithm. Some reconstructions with SRVP regularization [13]–[15] have shown isolated (groups of) cells that are attracted to a wrong VP-value. Note that those reconstructions were quite challenging, since only single frequency data were used. When the information content of the data is low with respect to the number of degrees of freedom [20], additional regularization is recommended.

This paper thus proposes to combine the non-spatial SRVP technique with a piecewise spatial smoothing technique. This combined technique, further denoted as Stepwise Relaxed Piecewise Smoothing Value Picking (SRPSVP) regularization, is more explicit in enforcing homogeneity within the image parts that are recognized to be so: it additionally imposes spatial smoothing within but not across a group of neighbor cells that are attracted to the same VP value. Note in this context also the approach in the Bayesian estimation framework presented in [21] for a finite number of dielectric and conductive materials, which applies a Gauss-Markov field for the distribution of the contrast with a hidden Potts-Markov field for the class of materials. Furthermore the presence of one-cell-artifacts can be strongly reduced if smoothing across such cells is allowed. Of course, this should be avoided in applications where the object actually contains small inclusions with the size of one cell.

The proposed method is discussed in Section III and illustrated in Section IV with permittivity reconstructions from the Institut Fresnel 2-D database [22], which contains multiple-frequency scattered field data for piecewise homogeneous objects from TM- and TE-polarized 2-D incident fields—only

Manuscript received June 11, 2012; manuscript revised December 05, 2012; accepted January 22, 2013. Date of publication March 07, 2013; date of current version May 29, 2013. This work was supported in part by a Ph.D. grant of the Institute for the Promotion of Innovation through Science and Technology in Flanders (IWT-Vlaanderen) SB/53079.

The authors are with the Department of Information Technology, Ghent University, B-9000 Gent, Belgium (e-mail: ann.franchois@intec.ugent.be).

Digital Object Identifier 10.1109/TAP.2013.2250472

single frequency data are used here. It is advantageous to employ the 2.5D forward scattering solver [23], since both polarization cases then can be computed with the same solver. Consequently, the inverse scattering problem is formulated in Section II for this more general 2.5D configuration, thus with 2-D material properties and 3D fields. An expression for the 2.5D field derivatives is derived in the Appendix.

II. The Electromagnetic Inverse Scattering Problem

Consider an inhomogeneous, possibly lossy, dielectric cylinder with an arbitrary cross-sectional shape and with the axis along the z-direction in a 3D cartesian coordinate system $\boldsymbol{\rho} = \mathbf{r} + z\mathbf{u}_z$, where $\mathbf{r} = x\mathbf{u}_x + y\mathbf{u}_y$. A 2-D rectangular investigation domain $\mathcal{D}$ is defined as the area in the cross-sectional x, y-plane where the (unknown) complex permittivity $\epsilon(\mathbf{r}) = \epsilon_0\epsilon_r(\mathbf{r}) + j\sigma(\mathbf{r})/\omega$ can differ from the free space permittivity ϵ_0. Here $\epsilon_r(\mathbf{r})$ is the relative dielectric permittivity, $\sigma(\mathbf{r})$ the conductivity and ω the angular frequency. To numerically solve the inverse problem, the unknown $\epsilon(\mathbf{r})$ is parameterized over $\mathcal{D}$ by approximating it as a piecewise constant function on a uniform grid with N^x and N^y identical square cells in, respectively, the x- and y-directions:

$$\epsilon(\mathbf{r}) \approx \sum_{m=0}^{N^x-1} \sum_{l=0}^{N^y-1} \epsilon_0\, \epsilon_{m,l}\, \Phi_{m,l}(\mathbf{r}), \quad \mathbf{r} \in \mathcal{D} \tag{1}$$

with $\Phi_{m,l}$ the unit expansion function and $\epsilon_{m,l}$ the unknown coefficients. The latter are gathered in the $N = N^xN^y$-dimensional relative complex permittivity vector $\boldsymbol{\epsilon}$, also $\{\epsilon_\nu\}$, $\nu = 1 \ldots N$. The input data of the inverse problem are a set of scattered fields $\mathbf{E}_i^s(\mathbf{r}_r, z_r) = \mathbf{E}_i(\mathbf{r}_r, z_r) - \mathbf{E}_i^i(\mathbf{r}_r, z_r)$, obtained by successively illuminating the scatterer with known incident fields $\mathbf{E}_i^i(\mathbf{r}, z)$, $i = 1 \ldots N^i$, and by measuring the corresponding total fields $\mathbf{E}_i(\mathbf{r}, z)$ in a set of receiver points $(\mathbf{r}_r, z_r)$, $r = 1 \ldots N^r$. A time dependency $\exp(-j\omega t)$ of the fields is assumed. The measured scattered fields are collected in the N^d-dimensional vector $\mathbf{e}^{meas}$, with $N^d = 3N^iN^r$, the factor 3 stands for the x, y, z components. The excitations are realized by (3D) angular diversity (N^t transmitter positions or propagation directions) and polarization diversity (N^p polarizations), hence $N^i = N^tN^p$, where for $N^p = 1$, TM- or TE- and for $N^p = 2$, TM- and TE-polarizations are applied.

The relation between the scattered field and the permittivity is governed by a non-linear integral equation [16]. The inverse problem thus is solved iteratively by minimizing a cost function $\mathcal{F}$, which consists of a data fit and regularization terms:

$$\mathcal{F}(\boldsymbol{\epsilon}, \mathbf{c}) = \mathcal{F}^{\mathcal{LS}}(\boldsymbol{\epsilon}) + \gamma\mathcal{F}^{\mathcal{P}}(\boldsymbol{\epsilon}, \mathbf{c}) + \zeta\mathcal{F}^{\mathcal{PS}}(\boldsymbol{\epsilon}) \tag{2}$$

with $\mathcal{F}^{\mathcal{P}}$ the VP regularizing function, $\mathbf{c}$ a P-dimensional vector ($P \ll N$) with the complex VP values c_p, $\mathcal{F}^{\mathcal{PS}}$ the Piecewise Smoothing (PS) regularizing function and γ and ζ positive regularization parameters. The least squares data fit,

$$\mathcal{F}^{\mathcal{LS}}(\boldsymbol{\epsilon}) = \frac{\|\mathbf{e}^{scat}(\boldsymbol{\epsilon}) - \mathbf{e}^{meas}\|^2}{\|\mathbf{e}^{meas}\|^2} \tag{3}$$

is a measure for the difference between the experimentally obtained scattered field and the corresponding simulated scattered field $\mathbf{e}^{scat}(\boldsymbol{\epsilon})$—also an N^d-dimensional vector—for the current value of $\boldsymbol{\epsilon}$, which is computed with a 2.5D volume integral equation solver [23].

III. Regularization and Optimization

A. The VP Regularization Term

The function $\mathcal{F}^{\mathcal{P}}$ is given by [13]

$$\mathcal{F}^{\mathcal{P}}(\boldsymbol{\epsilon}, \mathbf{c}) = \frac{1}{N}\sum_{\nu=1}^{N} f^P(|\epsilon_\nu - c_1|^2, \ldots, |\epsilon_\nu - c_P|^2) \tag{4}$$

where f^P is the P-dimensional choice function, defined as

$$f^P(u_1, \ldots, u_P) = F^P(u_1, \ldots, u_P; 0) \tag{5}$$

with $F^P(u_1, \ldots, u_P; x)$ defined through the recursion formula

$$F^P(u_1, \ldots, u_P; x) = (u_P + x)\,\frac{F^{P-1}(u_1, \ldots, u_{P-1}; x)}{F^{P-1}(u_1, \ldots, u_{P-1}; u_P + x)} \tag{6}$$

with $F^1(u_1; x) = u_1 + x$.

The function (4) can be reformulated as a weighted sum of penalty functions $|\epsilon_\nu - c_p|^2$ [13]:

$$\mathcal{F}^{\mathcal{P}}(\boldsymbol{\epsilon}, \mathbf{c}) = \frac{1}{N}\sum_{\nu=1}^{N}\sum_{p=1}^{P} b_{p,\nu}^P(\boldsymbol{\epsilon}, \mathbf{c})|\epsilon_\nu - c_p|^2. \tag{7}$$

The behavior of $\mathcal{F}^{\mathcal{P}}$ is as follows: (i) when the permittivity of a cell is close to one of the VP values, the choice function tries to enforce equality with this VP value (i.e., the corresponding weight b^P of that term in (7) is close to 1), (ii) when there is no clear preference of a permittivity cell for a particular VP value, no choice is made (b^P being somewhere intermediate between 0 and 1) and (iii) VP values that are clearly far away from the considered permittivity cell are neglected (their b^P are almost zero). Each VP value is initialized randomly (but different from already present VP values) within some predefined upper and lower bounds—the values of these bounds are not critical—and is updated in each iteration, see Section III-C, except for c_P, which is kept fixed to the background permittivity.

B. The PS Regularization Term

PS regularization penalizes permittivity fluctuations within but not across image parts that are considered—at a given iteration—to be homogeneous, further denoted as smoothing regions. Smoothing regions are derived from a mapping of the grid cells to VP-groups. A VP-group is the collection of cells that clusters around one VP value and is determined as follows: at a given iteration, the weights $b_{p,\nu}^P(\boldsymbol{\epsilon}, \mathbf{c})$ in (7) for cell ν indicate how close the permittivity of this cell is to each VP value c_p; the two largest weights for cell ν are compared and if their difference is larger than a threshold value (e.g., 0.2), then cell ν is assigned to the VP-group that corresponds with the largest weight; otherwise, it is assigned to the indefinite group. VP-groups (and also the indefinite group) can consist of several spatially disconnected image parts. A smoothing region is an as large as possible spatially connected group of cells belonging to one VP-group (or to the indefinite group).

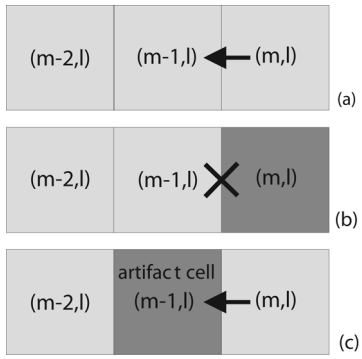

Fig. 1. Illustration of defining $\mathbf{S}^1_{m,l}$. Cells of the same color belong to the same VP-group. Allowed (arrow) and prohibited (cross) smoothing.

Whereas with multiplicative smoothing (MS) as in [3]—the cost function then is $\mathcal{F} = \mathcal{F}^{\mathcal{LS}}\left(1 + \alpha\mathcal{F}^{\mathcal{R}}\right)$, with α a positive regularization parameter—the regularizing function $\mathcal{F}^{\mathcal{R}}$ penalizes permittivity variations over all cell boundaries in the grid, $\mathcal{F}^{\mathcal{PS}}$ only does so over cell boundaries within each smoothing region. This is achieved by two matrices, $\mathbf{S}^1$ and $\mathbf{S}^2$ for the x- and y-directions, respectively,

$$\mathcal{F}^{\mathcal{PS}}(\boldsymbol{\epsilon}) = \frac{1}{\mathcal{N}^{\mathcal{R}}}\sum_{m=0}^{N^x}\sum_{l=0}^{N^y-1}\mathbf{S}^1_{m,l}\left|\epsilon_{m,l}-\epsilon_{m-1,l}\right|^2 + \frac{1}{\mathcal{N}^{\mathcal{R}}}\sum_{m=0}^{N^x-1}\sum_{l=0}^{N^y}\mathbf{S}^2_{m,l}\left|\epsilon_{m,l}-\epsilon_{m,l-1}\right|^2 \quad (8)$$

where $\mathcal{N}^{\mathcal{R}}$ is a normalization constant which accounts for the dimensions of the object and the size of the cells. If cell $(m-1,l)$ belongs to the same VP-group as cell (m,l), smoothing in the x-direction is allowed and $\mathbf{S}^1_{m,l}=1$, otherwise $\mathbf{S}^1_{m,l}=0$. This is also illustrated in Fig. 1(a) and (b), where cells having the same color are assigned to the same VP-group. Similarly, if cells $(m,l-1)$ and (m,l) belong to the same VP-group (or to the indefinite group), $\mathbf{S}^2_{m,l}=1$, otherwise $\mathbf{S}^2_{m,l}=0$. Note that the MS regularizing function $\mathcal{F}^{\mathcal{R}}$ is as (8) with all entries in $\mathbf{S}^1$ and $\mathbf{S}^2$ equal to 1. To smooth out one-cell-artifacts nested in a quasi-homogeneous image part, the second neighbor is taken into account. For example, if the neighbor cell $(m-1,l)$ does not belong to the same VP-group as cell (m,l) but cell $(m-2,l)$ does, it is assumed that cell $(m-1,l)$ was attracted to a wrong VP value, hence it is also allowed to smooth towards this cell and $\mathbf{S}^1_{m,l}=1$, see Fig. 1(c).

C. The Optimization

Each iteration k in the optimization of (2) is a three-step procedure. Firstly, the permittivity profile is updated from iteration k to $k+1$ as

$$\boldsymbol{\epsilon}_{k+1} = \boldsymbol{\epsilon}_k + \beta_k\mathbf{s}_k \quad (9)$$

where $\mathbf{s}_k$ is a Gauss-Newton descent direction and β_k is the step size which approximately minimizes the cost function $\mathcal{F}$ along this direction, computed with a line search [24]. During this step, the VP values $\mathbf{c}$ in $\mathcal{F}^{\mathcal{P}}$ and the smoothing matrices $\mathbf{S}^1$, $\mathbf{S}^2$ in $\mathcal{F}^{\mathcal{PS}}$ are kept fixed. The Gauss-Newton direction $\mathbf{s}_k$ for $\mathcal{F}$ is the solution of

$$\left(\mathbf{J}_k^H\mathbf{J}_k + \lambda^2\boldsymbol{\Sigma}_k\right)\mathbf{s}_k = -\left(\mathbf{J}_k^H\left[\mathbf{e}_k^{scat}-\mathbf{e}^{meas}\right] + \lambda^2\boldsymbol{\Omega}_k^*\right) \quad (10)$$

where λ^2 denotes $\|\mathbf{e}^{meas}\|^2$, $(\cdot)^H$ and $(\cdot)^*$ stand for conjugate transpose and complex conjugate, respectively and

$$\begin{aligned}\boldsymbol{\Omega}_k &= \gamma\,\boldsymbol{\Omega}_k^{\mathcal{P}} + \zeta\,\boldsymbol{\Omega}_k^{\mathcal{PS}}\\ \boldsymbol{\Sigma}_k &= \gamma\,\boldsymbol{\Sigma}_k^{\mathcal{P}} + \zeta\,\boldsymbol{\Sigma}_k^{\mathcal{PS}}.\end{aligned} \quad (11)$$

Equation (10) follows from the equation for the Newton correction in complex notation [25] for the cost function (2), by neglecting in the Hessian matrix the second order derivatives of the scattered field with respect to the permittivity unknowns, in a manner similar as in [13]. In the following, the subscript k is mostly omitted. Elements of the Jacobian matrix $\mathbf{J}$ are $\mathbf{J}_{n\nu} = \partial\left(\mathbf{e}^{scat}\right)_n/\partial\epsilon_\nu$, an expression is derived in the Appendix. $\boldsymbol{\Omega}^{\mathcal{P}}$ and $\boldsymbol{\Omega}^{\mathcal{PS}}$ contain the first order derivatives of the regularizing functions

$$\begin{aligned}\Omega_\nu^{\mathcal{P}*} &= \frac{\partial\mathcal{Q}^{\mathcal{P}}(\boldsymbol{\epsilon},\mathbf{c};\boldsymbol{\epsilon}_k,\mathbf{c}_k)}{\partial\epsilon_\nu^*}\\ &= \frac{1}{N}\sum_{p=1}^{P}b_{p,\nu}^P(\boldsymbol{\epsilon}_k,\mathbf{c}_k)(\epsilon_\nu-c_p) \quad (12)\\ \Omega_\nu^{\mathcal{PS}*} &= \frac{\partial\mathcal{F}^{\mathcal{PS}}}{\partial\epsilon_{m,l}^*}\\ &= \frac{1}{\mathcal{N}^{\mathcal{R}}}\Big[\mathbf{S}^1_{m,l}\left(\epsilon_{m,l}-\epsilon_{m-1,l}\right)+\mathbf{S}^2_{m,l}\left(\epsilon_{m,l}-\epsilon_{m,l-1}\right)\\ &\qquad +\mathbf{S}^1_{m+1,l}\left(\epsilon_{m,l}-\epsilon_{m+1,l}\right)\\ &\qquad +\mathbf{S}^2_{m,l+1}\left(\epsilon_{m,l}-\epsilon_{m,l+1}\right)\Big] \quad (13)\end{aligned}$$

where $\mathcal{Q}^{\mathcal{P}}$ is an approximation to $\mathcal{F}^{\mathcal{P}}$, obtained by considering the weights at their current values $b_{p,\nu}^P(\boldsymbol{\epsilon}_k,\mathbf{c}_k)$ as constants. $\boldsymbol{\Sigma}^{\mathcal{P}}$ and $\boldsymbol{\Sigma}^{\mathcal{PS}}$ contain the second order derivatives

$$\Sigma_{\nu,\mu}^{\mathcal{P}} = \frac{\partial^2\mathcal{Q}^{\mathcal{P}}(\boldsymbol{\epsilon},\mathbf{c};\boldsymbol{\epsilon}_k,\mathbf{c}_k)}{\partial\epsilon_\mu\partial\epsilon_\nu^*} = \delta_{\nu,\mu}\frac{1}{N}\sum_{p=1}^{P}b_{p,\nu}^P(\boldsymbol{\epsilon}_k,\mathbf{c}_k) \quad (14)$$

with $\delta_{i,j}$ the Kronecker symbol; for the diagonal elements

$$\begin{aligned}\Sigma_{\nu,\nu}^{\mathcal{PS}} &= \frac{\partial^2\mathcal{F}^{\mathcal{PS}}}{\partial\epsilon_{m,l}\partial\epsilon_{m,l}^*}\\ &= \frac{1}{\mathcal{N}^{\mathcal{R}}}\left[\mathbf{S}^1_{m,l}+\mathbf{S}^2_{m,l}+\mathbf{S}^1_{m+1,l}+\mathbf{S}^2_{m,l+1}\right] \quad (15)\end{aligned}$$

and for the non-diagonal elements (which are zero except if ν denotes a neighbor of μ)

$$\begin{aligned}\Sigma_{\nu,\mu}^{\mathcal{PS}} &= \frac{\partial^2\mathcal{F}^{\mathcal{PS}}}{\partial\epsilon_{p,q}\partial\epsilon_{m,l}^*}\\ &= -\frac{1}{\mathcal{N}^{\mathcal{R}}}\Big[\mathbf{S}^1_{m,l}\delta_{p,m-1}\delta_{q,l}+\mathbf{S}^2_{m,l}\delta_{p,m}\delta_{q,l-1}\\ &\qquad +\mathbf{S}^1_{m+1,l}\delta_{p,m+1}\delta_{q,l}\\ &\qquad +\mathbf{S}^2_{m,l+1}\delta_{p,m}\delta_{q,l+1}\Big]. \quad (16)\end{aligned}$$

Note that with MS regularization (used as a benchmark in Section IV) the employed modified Gauss-Newton direction satisfies an equation as (10) with $\mathbf{\Omega}_k = \mathbf{\Omega}_k^{\mathcal{R}}$, $\mathbf{\Sigma}_k = \mathbf{\Sigma}_k^{\mathcal{R}}$ and $\lambda^2 = \alpha\|\mathbf{e}^{meas}\|^2\mathcal{F}_k^{\mathcal{LS}}/(1+\alpha\mathcal{F}_k^{\mathcal{R}})$ [3].

Secondly, the VP values $\{c_p\}$ are updated, while the permittivity and smoothing matrices are kept fixed. Since they are subject to upper and lower bounds on their real and imaginary parts, a constrained optimization is performed by an active set method [24], which acts on $\mathcal{F}^{\mathcal{P}}$ only. Similarly as with SRVP regularization, VP values are also updated whenever a new VP value is introduced.

Thirdly, the VP-groups/indefinite group and next the smoothing matrices $\mathbf{S}^1$ and $\mathbf{S}^2$ are updated, see Section III-B. The iterations are stopped when the data fit reaches the noise level, $\mathcal{F}^{\mathcal{LS}} \approx T^N$. The noise level $T^N = \mathcal{F}^{\mathcal{LS}}(\epsilon^0)$ is defined as the data fit for ϵ^0, which is the discretized permittivity profile that yields the closest approximation to the true profile.

With *MS regularization* it was observed [3] that the data fit is able to reach T^N with choices of the regularization parameter α in a wide range of values and that $\mathcal{F}^{\mathcal{LS}}$ is not much further minimized once this happens; a rather large α in this range yields an appropriately smoothed reconstruction, see the discrepancy principle [26].

With *SRVP regularization* the iterations start with only one VP value (strong regularization) and proceed until a local minimum of the corresponding cost function $\mathcal{F}$ is reached (i.e., its gradient is small) or until $\mathcal{F}^{\mathcal{LS}}$ increases again. For a sufficiently large regularization parameter γ, this first step terminates with $\mathcal{F}^{\mathcal{LS}} > T^N$. The regularization then is relaxed by adding an extra VP value and the optimization proceeds as before. New VP values are added this way until $\mathcal{F}^{\mathcal{LS}}$ reaches (an estimate of) T^N. Ideally, $P = P_0$ at this stage, with P_0 the number of different permittivity values in the exact profile, but when γ is chosen too large, the algorithm typically stops with $P > P_0$; some of these VP values tend to merge such that still a satisfactory reconstruction is obtained. When γ is too small, $\mathcal{F}^{\mathcal{LS}}$ easily reaches T^N, even with too few VP values, but the reconstruction then is of poorer quality.

In this paper, the choice of γ results from numerical experimentation, but *a priori* knowledge of the exact profile—apart from its piecewise-homogeneous character with $P_0 \ll N$—is not assumed: if the final reconstruction shows insufficient clustering of the permittivity unknowns around the VP values, a larger γ is tried; if the clustering is sufficient, a smaller γ can be tried to see if a comparable clustering can be achieved with fewer VP values and/or with fewer iterations. We did not perform an in-depth study on the choice of the parameters γ and ζ in case of *SRPSVP regularization*. In the examples of Section IV, γ is chosen as with the SRVP regularization case and ζ as with the MS regularization.

IV. Reconstructions From Experimental Data

A. Objects, Measurement Set-Up and General Settings

Single frequency scattering data at 4 GHz ($\lambda_0 = 74.9$ mm) are considered for two objects from the Institut Fresnel 2-D database [22]: the *FoamDielExt* object, which consists of a plastic cylinder with radius $r_a = 15.5\,\text{mm} \approx 0.2\lambda_0$ and relative permittivity $\epsilon_{r,a} = 3 \pm 0.3$ that is placed against a foam cylinder with $r_b = 40$ mm $\approx 0.5\lambda_0$ and $\epsilon_{r,b} = 1.45 \pm 0.15$ (Fig. 3(a)) and the *FoamTwinDiel* object, which is as *FoamDielExt* plus an extra plastic cylinder off-centered inside the foam cylinder, with their centers 5 mm apart (Fig. 3(e)).

The illumination—receiver configuration, with 360 (1° spaced) possible antenna positions on a circle with radius 1.67 m in the xy-plane, is detailed in [27]. Here, we use a subset of 8 (45° spaced) transmitter positions for *FoamDielExt* and 18 (20° spaced) positions for *FoamTwinDiel*, and 241 receiving antenna positions on an arc (from 60° to 300°) facing the source (when at 0°). We invert both TM and TE data simultaneously, whence separate inversions are presented in [28], the only contribution in [22] that exploits both polarizations for the considered objects. This means that we include both polarizations in the field vectors $\mathbf{e}^{meas}$ and $\mathbf{e}^{scat}$ in (3), e.g., by filling each vector first with the TE-data followed by the TM-data. Since the fields in this paper are considered purely 2-D [27], all TM-fields are parallel to the z-axis, in particular $\mathbf{E}^{s,\mathrm{TM}} = E_z^{s,\mathrm{TM}}\mathbf{u}_z$, $E_x^{s,\mathrm{TM}} = 0$, $E_y^{s,\mathrm{TM}} = 0$, and all TE-fields are parallel to the xy-plane, in particular $\mathbf{E}^{s,\mathrm{TE}} = E_x^{s,\mathrm{TE}}\mathbf{u}_x + E_y^{s,\mathrm{TE}}\mathbf{u}_y$, $E_z^{s,\mathrm{TE}} = 0$ (the TE scattered field furthermore is tangential to the measurement circle). For this configuration, the 2.5D solver [23] solves both polarization cases at once, if the incident field is chosen as the sum of the TE and TM incident fields at a given source position, i.e., $\mathbf{E}^i = E_x^{i,\mathrm{TE}}\mathbf{u}_x + E_y^{i,\mathrm{TE}}\mathbf{u}_y + E_z^{i,\mathrm{TM}}\mathbf{u}_z$ yields $\mathbf{E}^s = E_x^{s,\mathrm{TE}}\mathbf{u}_x + E_y^{s,\mathrm{TE}}\mathbf{u}_y + E_z^{s,\mathrm{TM}}\mathbf{u}_z$. The dimension of the data vector $\mathbf{e}^{meas}$ then is $N^d = 3N^tN^r = 5784$ complex numbers for *FoamDielExt* and $N^d = 13014$ for *FoamTwinDiel*. A simple calibration is applied to match phase and energy between measured and simulated fields [27]: all measured field values are multiplied by a complex factor, which is the ratio of the simulated and measured incident fields at the receiver location opposite to the source. The incident fields are treated as plane waves.

In each experiment, the foam cylinder was positioned in the center of the antenna circle (within the positioning uncertainty), which is also the center of the reconstruction grid. This grid is a 150 mm × 150 mm square, that is discretized in 30 × 30 square cells with edge 5 mm (roughly 15 cells per λ_0), yielding a total of 900 permittivity unknowns. This relatively small cell size should facilitate the reconstruction of the curved object contours. For the forward problem solution, each cell is subdivided further in $2 \times 2 = 4$ forward problem cells, the tolerance for the BICGSTAB routine is set to 10^{-3} [23] and a marching-on-in-source-position approach [29] using three previous solutions is applied. Since the fields are 2-D, the 2.5D computations only need to be done for one Fourier component $k_z = 0$.

During the reconstructions, constraints are imposed on the VP values but not on the permittivity profile. They are $1.1 < \Re(c_p) < 5$ and $-0.001 < \Im(c_p) < 0.001$, $p = 1 \ldots P-1$, knowing that the permittivities under test do not have a significant imaginary part. Consequently, most figures in this paper only show the real part of the permittivity (see [15] for the imaginary parts). The iterations are stopped when the data fit reaches $\mathcal{F}^{\mathcal{LS}} = 5\ 10^{-3}$ or as soon as a sixth extra VP value is to be

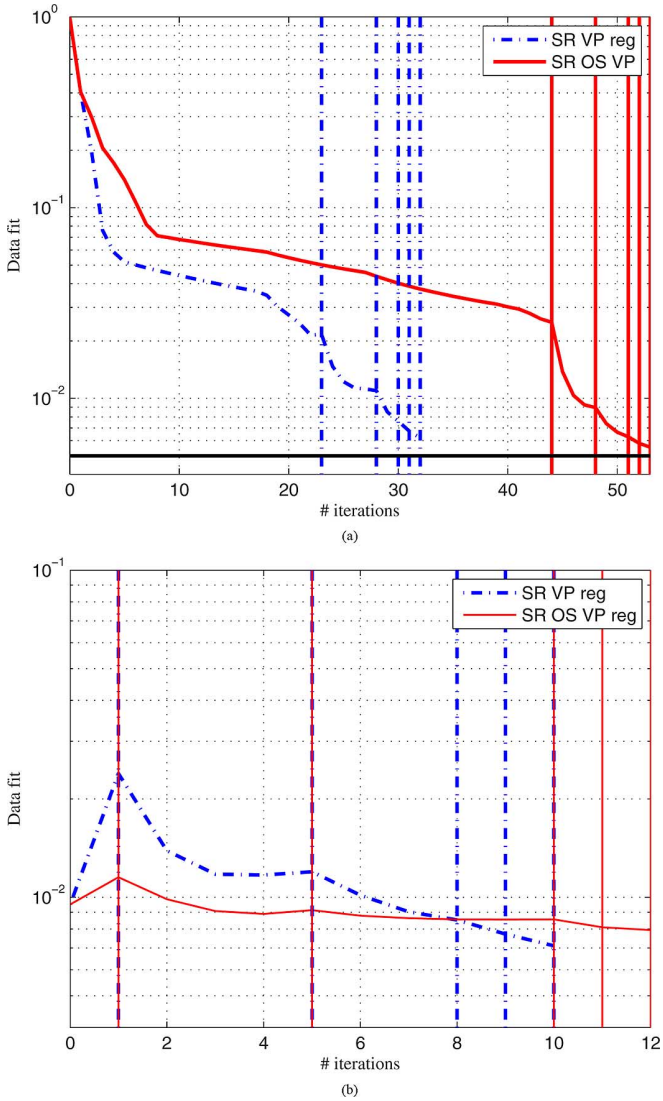

Fig. 2. Data fit $\mathcal{F}^{\mathcal{LS}}$ as a function of the iteration number: SRVP (dash-dots), SRPSVP (solid). Vertical lines indicate when a VP value was added. (a) *FoamDielExt* (b) *FoamTwinDiel*.

introduced. All computations are performed on a machine with two AMD Opteron 270 Quad core processors occupying all 8 CPU cores (each core solves a set of forward problems). In the following, reconstructions with MS, SRVP and SRPSVP regularization are discussed.

B. Reconstructions of FoamDielExt

For all the reconstructions of *FoamDielExt* a free space grid is chosen as the initial permittivity estimate. First a reconstruction with *MS regularization* is performed with a regularization parameter $\alpha = 2\ 10^{-3}$. Fig. 3(b) shows the result after 16 iterations, when the data fit stagnates around $\mathcal{F}^{\mathcal{LS}} = 1.4\ 10^{-3}$. The plastic cylinder is clearly visible and its permittivity is well estimated (approximately 3), but the foam cylinder is rather blurry without a clear shape or permittivity and artifacts are present in the background. Due to the globally imposed smoothness, permittivities are not well clustered.

Next a reconstruction with *SRVP regularization* is performed with $\gamma = 3$ and $\zeta = 0$ in (2). It was observed that with $\gamma = 1$ the data fit decreased too fast, leaving insufficient influence for the regularization, while with $\gamma = 5$ convergence was too slow. The reconstruction is obtained after 32 iterations (3 h 40 min), see Fig. 2(a). The algorithm adds more VP values than there are materials (in the last iterations a new VP value is introduced in each step), but most of these end up merging or approaching one another. The final VP values are $c_1 = 2.99$, $c_2 = 1.39$, $c_3 = c_4 = 2.70$ and $c_5 = 2.8$. They all lie within the specified uncertainties on the object properties ($\epsilon_{r,a} = 3 \pm 0.3$ and $\epsilon_{r,b} = 1.45 \pm 0.15$). None of the weights (7) corresponding with c_1, c_3, c_4 and c_5 are dominant, but the cells of the plastic cylinder are slightly more attracted to $c_3 = 2.70$, which may explain why the cylinder dimensions are somewhat overestimated, see Fig. 3(c). Some artifacts are clearly visible in the three permittivity regions: cells in the plastic cylinder pick the VP value corresponding to the foam cylinder and vice versa; a similar exchange of VP values is observed for the background and foam. These artifacts also appear in the dash-dot curves in Fig. 4, which show the permittivity along lines parallel to the x- and y- axes of the grid at $y = -5$ mm and $x = -5$ mm respectively.

Let us therefore apply the proposed *SRPSVP regularization*, with $\gamma = 3$ and $\zeta = 2\ 10^{-3}$ ($\mathcal{N}^{\mathcal{R}} = 1$). Compared to the SRVP cost function, the weight of the regularizing terms relative to the data fit term has increased, resulting in a slower decrease of the data fit, see Fig. 2(a). Consequently, VP values are added later in the optimization process. The final VP values (after 53 iterations) are $c_1 = 3.00$, $c_2 = 1.48$ and $c_3 = c_4 = c_5 = 2.75$. They fit even better within the uncertainties on the object properties than those obtained with SRVP. None of the weights corresponding with c_1, c_3, c_4, c_5 are dominant, hence all cells within the plastic cylinder end up in the indefinite group and the smoothing is performed over this complete cylinder. Also the cells in almost the exact foam cylinder contour belong to the same VP-group. The reconstructed permittivity profile in Fig. 3(d) shows that most artifacts of Fig. 3(c) have disappeared. Dimensions and positions of both cylinders are correctly reconstructed and the shapes are better than with SRVP regularization alone. The dashed curves in Fig. 4 show that the permittivity of the foam cylinder is accurately reconstructed while that of the plastic cylinder is somewhat underestimated.

C. Reconstructions of FoamTwinDiel

A reconstruction with *MS regularization* is performed, with $\alpha = 2\ 10^{-3}$ and starting from a free space permittivity grid. Fig. 3(f) shows the result after 22 iterations, when $\mathcal{F}^{\mathcal{LS}} = 2.4\ 10^{-3}$. The presence of the two plastic cylinders is clearly visible, although their shape is harder to determine. As with *FoamDielExt* the foam cylinder is less perceptible and there are fluctuations in the background.

Next a reconstruction with *SRVP regularization* is performed with $\gamma = 3$ and $\zeta = 0$ in (2). Since the number of transmitters now is about twice that for *FoamDielExt*, resulting in a longer computation time, the initial permittivity is chosen as the available profile at iteration 5 of the MS reconstruction, see Fig. 5 (with $\mathcal{F}^{\mathcal{LS}} = 9.5\ 10^{-3}$ after 2 h 30 min). Note that the final result of Fig. 3(f) cannot be used since the corresponding data

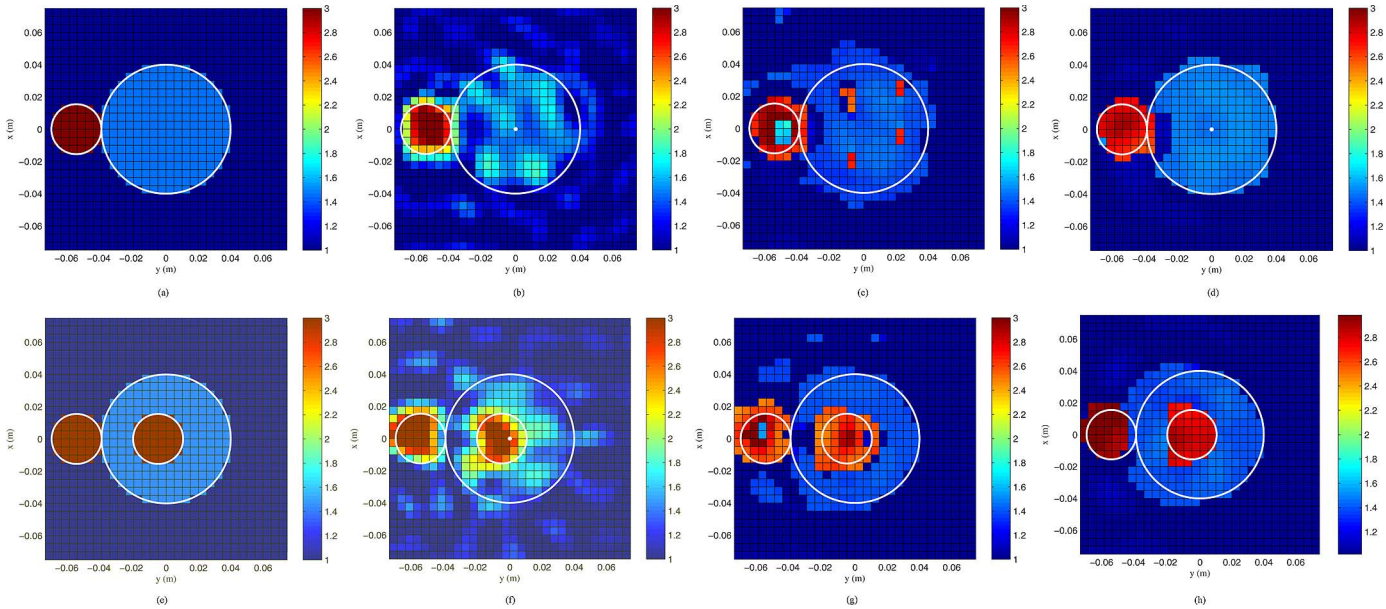

Fig. 3. Real part of the permittivity for *FoamDielExt* (a)–(d): exact (a), reconstructions with MS (b), SRVP (c), SRPSVP (d) and for *FoamTwinDiel* (e)–(g): exact (e), reconstructions with MS (f), SRVP (g), SRPSVP (h). The white lines indicate the actual object contours.

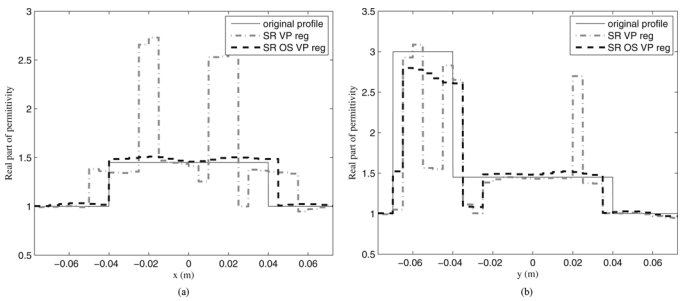

Fig. 4. Real part of the reconstructed permittivity along x- and y-directions for *FoamDielExt*. Solid: exact profiles from Fig. 3(a), Dash-dots: SRVP profiles from Fig. 3(c), Dashes: SRPSVP profiles from Fig. 3(d). (a) Along x at $y = -5$ mm. (b) Along y at $x = -5$ mm.

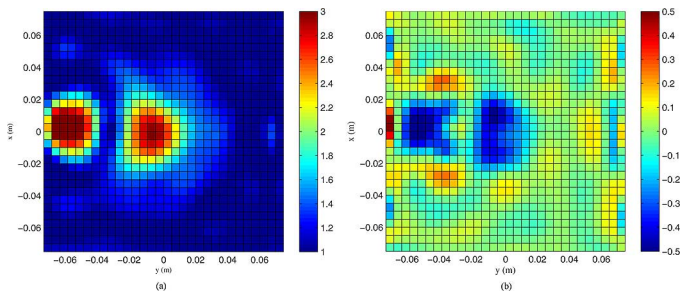

Fig. 5. Initial estimate for the reconstructions of *FoamTwinDiel* with SRVP and SRPSVP. (a) Real part. (b) Imaginary part.

fit is on the noise level and leaves no room for further optimization. The reconstruction is obtained after 10 iterations (3 h 35 min), see Fig. 2(b). The VP values then are given by $c_1 = 3.00$, $c_2 = 1.39$ and $c_3 = c_4 = c_5 = 2.59$. The values c_1 and c_2 lie well within the uncertainties on the object properties, while $c_3 = c_4 = c_5$ are slightly too low. However, the clustering of the permittivities (Fig. 3(g)) compared to the MS reconstruction (Fig. 3(f)) is apparent. As with *FoamDielExt* artifacts are visible in all permittivity regions: cells in the plastic cylinders pick VP values corresponding to the foam cylinder and background and vice versa. Fig. 7 shows cross-sections along the x- and y- axis and through the center of the reconstruction grid.

Let us again apply SRPSVP with $\gamma = 3$ and $\zeta = 2\ 10^{-3}$. The final VP values after 12 iterations are $c_1 = 3.50$, $c_2 = 1.40$ and $c_3 = c_4 = c_5 = 2.88$. Fig. 6 shows the VP-groups mapping at some iterations when a new VP value is added. It follows that no cells finally are attracted to $c_1 = 3.50$ (Fig. 6(d)). However, the introduction of c_1 has not been useless, as appears from Fig. 6(a), when $c_1 = 3.03$ and the two plastic cylinders start to appear at the correct locations. After introducing $c_2 = 1.34$ (Fig. 6(b)), the foam cylinder also appears at the correct position. In Fig. 6(d), all cells at the location of the plastic cylinders pick $c_3 = c_4 = c_5 = 2.88$ and belong to the indefinite

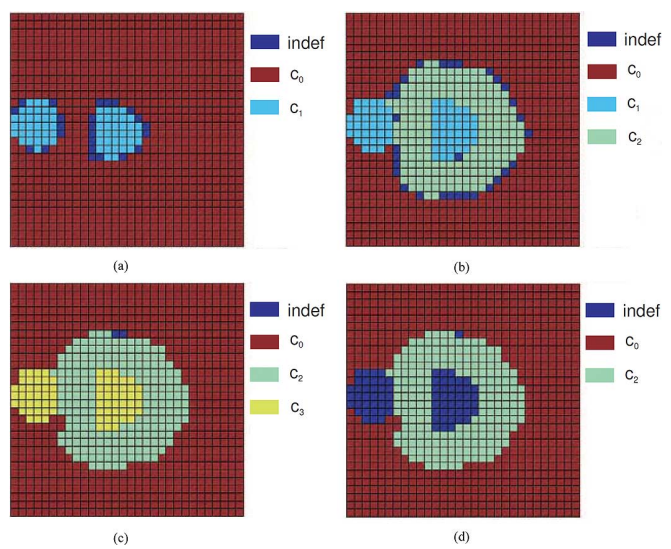

Fig. 6. Mapping of the permittivity cells into VP-groups at different iterations (it.) during the reconstruction of *FoamDielTwin*. Each VP-group is represented by its VP value, c_0 stands for the fixed background VP value and *indef* for the indefinite group. (a) it. 1: $c_1 = 3.03$. (b) it. 5: $c_2 = 1.34$. (c) it. 10: $c_3 = 2.92$. (d) it. 11: $c_4 = c_3 = 2.88$.

group, while those located in the foam cylinder are attracted to $c_2 = 1.40$. We can conclude that also for *FoamTwinDiel*

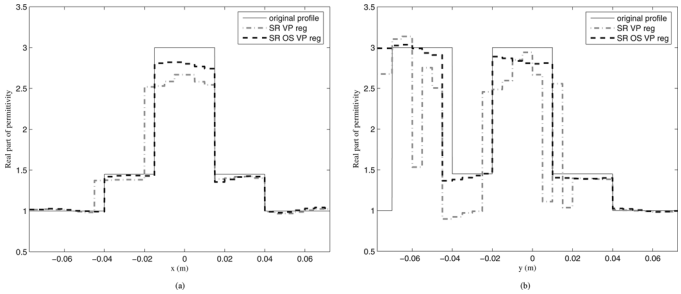

Fig. 7. Real part of the reconstructed permittivity along x- and y-directions for *FoamTwinDiel*. Solid: exact profiles from Fig. 3(e), Dash-dots: SRVP profiles from Fig. 3(g), Dashes: SRPSVP profiles from Fig. 3(h). (a) along x at $y = 0$ mm. (b) along y at $x = 0$ mm.

the smoothing is performed in the appropriate regions. The reconstructed permittivity in Fig. 3(h) shows that the artifacts of Fig. 3(g) have disappeared. The reconstruction quality is comparable to that of Fig. 3(d): shape, dimensions and positions of all cylinders are correctly reconstructed, except for a slight translation (approximately two cells) of the foam cylinder to the left. The dashed curves in Fig. 7 show that the permittivities of the foam and exterior plastic cylinders are almost exactly reconstructed while the permittivity of the inner plastic cylinder is somewhat underestimated.

Concluding, the combination of piecewise smoothing with SRVP regularization can significantly improve the results compared to applying SRVP regularization alone. The reconstructions obtained here from single frequency data visibly are of superior quality than those presented in [22] for the same objects and also using single frequency data, e.g., with a multi-resolution inversion technique [30]. They even are comparable to and in many cases better than the reconstructions from multi-frequency or frequency-hopping data in [22], see e.g., with n-ary level-sets [11], with an adaptive multiscale approach [31], with a frequency-weighted data fit cost function [32], with an extended Born inversion with Tikonov regularization [33], with multiplicative weighted TV regularized contrast source inversion (CSI) [28], with a diagonal tensor approximation CSI [34], and with compound Markov modelling [21]. Compared to the weighted L2-norm TV regularization applied to CSI in [28] or applied to a hybrid technique in [35], both using multi-frequency data, the SRPSVP regularization yields sharper edges, especially for the foam cylinders in [28] and for the plastic cylinder in [35]. Also in the 3D case, edges are clear when using SRVP regularization [14] while some smoothing is observed with weighted L2-norm TV regularization [36]. A possible explanation is that with SRPSVP regularization, the smoothing strength is set equal to zero across cell boundaries that are assumed, at a given iteration, to coincide with edges, while with L2-norm TV regularization, the spatially dependent smoothing weights then are small but still non-zero. Therefore, SRPSVP regularization may present advantages compared to TV when dealing with piecewise constant objects.

V. Conclusion

In this contribution we have presented a regularization strategy for piecewise (quasi-)homogeneous objects, that combines a non-spatial value picking regularization method with a piecewise spatial smoothing regularization. In each iteration of the optimization scheme, the VP values provided by the former serve to determine the separate smoothing regions in the image for the latter. The new method is validated by reconstructions of real world objects from experimental data. In particular reconstructions from single-frequency TM- and TE-polarized scattering data from the Institut Fresnel 2-D database were presented for two piecewise homogeneous objects, *FoamDielExt* and *FoamTwinDiel*. These reconstructions are quite accurate and show a significant improvement compared to those obtained with the non-spatial technique only or with a global spatial smoothing approach. They also compare well to reconstructions of the same objects with various techniques by other authors. It can be concluded that SRPSVP is indeed a valuable approach to deal with artifacts that may appear when SRVP only is applied to piecewise (quasi-)homogeneous objects.

Appendix
Scattered Field Derivatives

A closed form expression is derived for the scattered field derivatives $\partial \mathbf{E}^s(\mathbf{r}, z)/\partial \epsilon_\nu$. In the 2.5D formulation [23] Fourier field expansions are employed, hence the derivative is written as

$$\frac{\partial \mathbf{E}^s(\mathbf{r}, z)}{\partial \epsilon_\nu} = \frac{1}{2\pi} \int_{-\infty}^{\infty} \frac{\partial \widehat{\mathbf{E}}^s(\mathbf{r}, k_z)}{\partial \epsilon_\nu} e^{jk_z z} dk_z \tag{17}$$

where $\widehat{\cdot}$ stands for the Fourier transform,

$$\widehat{g}(\mathbf{r}, k_z) = \int_{-\infty}^{\infty} g(\mathbf{r}, z) e^{-jk_z z} dz. \tag{18}$$

An operator $\mathcal{G}^{\mathcal{V}}$ acting on a vector function $\mathbf{p}$ with support $\mathcal{V}$ is defined as

$$[\mathcal{G}^{\mathcal{V}}(\mathbf{p})](\mathbf{r}) = j\omega\mu_0 \left(\mathbf{I} + \frac{1}{k_0^2} \widehat{\nabla}\widehat{\nabla} \right) \cdot \int_{\mathcal{V}} \widehat{G}(\mathbf{r}, \mathbf{r}'; k_z) \mathbf{p}(\mathbf{r}') d\mathbf{r}' \tag{19}$$

where $\mathbf{I}$ is the 3×3 identity dyadic, $\widehat{\nabla} = ((\partial/\partial x), (\partial/\partial y), jk_z)$ and

$$\widehat{G}(\mathbf{r}, \mathbf{r}'; k_z) = \frac{j}{4} H_0^{(1)} \left(\sqrt{k_0^2 - k_z^2} \, |\mathbf{r} - \mathbf{r}'| \right) \tag{20}$$

which corresponds to the 2-D scalar Green's function of homogeneous space with relative permittivity $\epsilon_r = 1 - k_z^2/k_0^2$. The CSIE [23] for the total field $\widehat{\mathbf{E}}(\mathbf{r}, k_z)$ then is formulated as

$$\widehat{\mathbf{E}}(\mathbf{r}, k_z) = [\mathcal{G}^{\mathcal{S}}(\widehat{\mathbf{J}}^i)](\mathbf{r}) + [\mathcal{G}^{\mathcal{D}}(-j\omega[\epsilon - \epsilon_0]\widehat{\mathbf{E}})](\mathbf{r}) \tag{21}$$

where $\mathbf{J}^i$ and $-j\omega[\epsilon - \epsilon_0]\widehat{\mathbf{E}}$ are the applied and induced current densities, respectively. Since the incident field does not depend on the permittivity, derivation of (21) and using (1) yields

$$\frac{\partial \widehat{\mathbf{E}}^s(\mathbf{r}, k_z)}{\partial \epsilon_\nu} = [\mathcal{G}^{\mathcal{D}}(-j\omega\epsilon_0 \Phi_\nu \widehat{\mathbf{E}})](\mathbf{r}) + [\mathcal{G}^{\mathcal{D}}(-j\omega[\epsilon - \epsilon_0] \frac{\partial \widehat{\mathbf{E}}^s(\mathbf{r}, k_z)}{\partial \epsilon_\nu})](\mathbf{r}). \tag{22}$$

Comparing (22) with (21), it follows that $\partial \widehat{\mathbf{E}}^s(\mathbf{r}, k_z)/\partial \epsilon_\nu$ satisfies an equation as (21) corresponding to an applied current

density $-j\omega\epsilon_0\Phi_\nu\widehat{\mathbf{E}}$ in cell ν. Consequently, an expression is readily obtained from the total field solution of (21) when it is expressed as a function of $\widehat{\mathbf{J}}^i$, by replacing $\widehat{\mathbf{J}}^i$ with $-j\omega\epsilon_0\Phi_\nu\widehat{\mathbf{E}}$. Therefore the 3×3 dyadic Green's function of inhomogeneous space $\widehat{\mathbf{G}}_{\rm inh}(\mathbf{r},\mathbf{r}';k_z)$ is constructed by applying a 2-D elementary dipole current density

$$\widehat{\mathbf{J}}_{\delta,p}(\mathbf{r}-\mathbf{r}')=\frac{1}{j\omega\mu_0}\delta(\mathbf{r}-\mathbf{r}')\mathbf{u}_p \tag{23}$$

along a unit vector $\mathbf{u}_p$ in a point $\mathbf{r}'$ in presence of the scatterer for the three orthogonal directions $p=x,y,z$. The resulting total fields $\widehat{\mathbf{E}}_p^{\rm dipole}$ yield the columns of the inhomogeneous dyadic Green's function

$$\begin{aligned}\widehat{\mathbf{E}}_p^{\rm dipole}(\mathbf{r},k_z)&=j\omega\mu_0\int_{\mathcal{D}}\widehat{\mathbf{G}}_{\rm inh}(\mathbf{r},\mathbf{r}'';k_z)\cdot\widehat{\mathbf{J}}_{\delta,p}(\mathbf{r}''-\mathbf{r}')d\mathbf{r}''\\&=\widehat{\mathbf{G}}_{\rm inh}(\mathbf{r},\mathbf{r}';k_z)\cdot\mathbf{u}_p.\end{aligned} \tag{24}$$

The total field resulting from the current density $\widehat{\mathbf{J}}^i(\mathbf{r},k_z)$ in presence of the scatterer then is expressed as

$$\widehat{\mathbf{E}}(\mathbf{r},k_z)=j\omega\mu_0\int_{\mathcal{D}}\widehat{\mathbf{G}}_{\rm inh}(\mathbf{r},\mathbf{r}';k_z)\cdot\widehat{\mathbf{J}}^i(\mathbf{r}',k_z)d\mathbf{r}'. \tag{25}$$

It follows that

$$\frac{\partial\widehat{\mathbf{E}}^s(\mathbf{r},k_z)}{\partial\epsilon_\nu}=k_0^2\int_{\mathcal{D}}\Phi_\nu(\mathbf{r}')\widehat{\mathbf{G}}_{\rm inh}(\mathbf{r},\mathbf{r}';k_z)\cdot\widehat{\mathbf{E}}(\mathbf{r}',k_z)d\mathbf{r}'. \tag{26}$$

Now the elements $\mathbf{E}^s_{t,p}(\mathbf{r}_r,z_r)\cdot\mathbf{u}_{r,p'}$ of the scattered field vector $\mathbf{e}^{scat}$ are considered. These are the x,y,z scattered field components in receiver points $(\mathbf{r}_r,z_r)$ resulting from illuminations $E^i_{t,p}\mathbf{u}_{t,p}$. It follows that

$$\begin{aligned}\frac{\partial\widehat{\mathbf{E}}^s_{t,p}}{\partial\epsilon_\nu}(\mathbf{r}_r,k_z)\cdot\mathbf{u}_{r,p'}&=k_0^2\int_{\mathcal{D}}\Phi_\nu(\mathbf{r}')\,\mathbf{u}_{r,p'}\cdot\widehat{\mathbf{G}}_{\rm inh}(\mathbf{r}_r,\mathbf{r}';k_z)\\&\quad\cdot\widehat{\mathbf{E}}_{t,p}(\mathbf{r}',k_z)d\mathbf{r}'.\end{aligned} \tag{27}$$

Due to reciprocity $\widehat{\mathbf{G}}_{\rm inh}(\mathbf{r}_r,\mathbf{r}';k_z)=\widehat{\mathbf{G}}^T_{\rm inh}(\mathbf{r}',\mathbf{r}_r;k_z)$ and from (24) it follows that

$$\begin{aligned}\mathbf{u}_{r,p'}\cdot\widehat{\mathbf{G}}_{\rm inh}(\mathbf{r}_r,\mathbf{r}';k_z)&=\widehat{\mathbf{G}}_{\rm inh}(\mathbf{r}',\mathbf{r}_r;k_z)\cdot\mathbf{u}_{r,p'}\\&=\widehat{\mathbf{E}}^{\rm dipole}_{r,p'}(\mathbf{r}',k_z).\end{aligned} \tag{28}$$

Here, $\widehat{\mathbf{E}}^{\rm dipole}_{r,p'}(\mathbf{r}',k_z)$ is the total field generated by a 2-D dipole in the point $\mathbf{r}_r$ oriented along $\mathbf{u}_{r,p'}$ in presence of the scatterer. Introducing (28) into (27) finally yields

$$\begin{aligned}&\frac{\partial\widehat{\mathbf{E}}^s_{t,p}}{\partial\epsilon_\nu}(\mathbf{r}_r,k_z)\cdot\mathbf{u}_{r,p'}\\&\quad=k_0^2\int_{\mathcal{D}}\Phi_\nu(\mathbf{r}')\,\widehat{\mathbf{E}}_{t,p}(\mathbf{r}',k_z)\cdot\widehat{\mathbf{E}}^{\rm dipole}_{r,p'}(\mathbf{r}',k_z)d\mathbf{r}'.\end{aligned} \tag{29}$$

To compute (29), two types of forward problems must be solved for each spectral component k_z of the incident field: (i) a *regular* forward problem to compute $\widehat{\mathbf{E}}_{t,p}(\mathbf{r}',k_z)$ on $\mathcal{D}$ for each incidence (t,p), or a total of $\#k_zN^tN_t^p$ forward problems; these have been solved already to determine the data fit term (3); (ii) a *dipole* forward problem to compute $\widehat{\mathbf{E}}^{\rm dipole}_{r,p'}(\mathbf{r}',k_z)$ on $\mathcal{D}$ for dipole excitations in each receiver position $\mathbf{r}_r$, or a total of $\#k_zN^rN_r^p$ forward problems.

REFERENCES

[1] A. G. Tijhuis, K. Belkebir, A. Litman, and B. P. de Hon, "Theoretical and computational aspects of 2-D inverse profiling," *IEEE Trans. Geosci. Remote Sens.*, vol. 39, no. 6, pp. 1316–1330, Jun. 2001.

[2] A. Franchois and A. G. Tijhuis, "A quasi-Newton reconstruction algorithm for a complex microwave imaging scanner environment," *Radio Sci.*, vol. 38, no. 2, pp. 8011–13, Jan. 2003.

[3] J. De Zaeytijd, A. Franchois, C. Eyraud, and J. M. Geffrin, "Full-wave three-dimensional microwave imaging with a regularized Gauss-Newton method—Theory and experiment," *IEEE Trans. Antennas Propag.*, vol. 55, no. 11, pp. 3279–3292, Nov. 2007.

[4] Y. Deng and X. Liu, "Electromagnetic imaging methods for nondestructive evaluation applications," *Sensors*, vol. 11, pp. 11774–11808, Dec. 2011.

[5] F. Soldovieri and R. Solimene, "Ground penetrating radar subsurface imaging of buried objects," in *Radar Technology* , G. Kouemou, Ed. New York, NY, USA: InTech, 2010 [Online]. Available: http://www.intechopen.com/books/radar-technology/ground-penetrating-radar-subsurface-imaging-of-buried-objects

[6] P. M. Van den Berg and R. E. Kleinman, "A total variation enhanced modified gradient algorithm for profile reconstruction," *Inverse Prob.*, vol. 11, no. 3, pp. L5–L10, Jun. 1995.

[7] P. Charbonnier, L. Blanc-Féraud, G. Aubert, and M. Barlaud, "Deterministic edge-preserving regularization in computed imaging," *IEEE Trans. Image Process.*, vol. 6, no. 2, pp. 298–311, Feb. 1997.

[8] P. M. Van den Berg and A. Abubakar, "Contrast source inversion method: State of art," *Progress Electromagn. Res.*, vol. 34, pp. 189–218, 2001.

[9] P. Lobel, L. Blanc-Féraud, C. Pichot, and M. Barlaud, "A new regularization scheme for inverse scattering," *Inverse Prob.*, vol. 13, pp. 403–410, 1997.

[10] A. Baussard, D. Prémel, and O. Venard, "A Bayesian approach for solving inverse scattering from microwave laboratory-controlled data," *Inverse Prob.*, vol. 17, no. 6, pp. 1659–1669, Dec. 2001.

[11] A. Litman, "Reconstruction by level sets of n-ary scattering obstacles," *Inverse Prob.*, vol. 21, no. 6, pp. S131–S152, Dec. 2005.

[12] O. Dorn and D. Lesselier, "Level set methods for inverse scattering—Some recent developments," *Inverse Prob.*, vol. 25, no. 12, pp. 125001–125001, 2009.

[13] J. De Zaeytijd, A. Franchois, and J. M. Geffrin, "A new value picking regularization strategy—Application to the 3D electromagnetic inverse scattering problem," *IEEE Trans. Antennas Propag.*, vol. 57, no. 4, pp. 1133–1149, Apr. 2009.

[14] J. De Zaeytijd and A. Franchois, "Three-dimensional quantitative microwave imaging from measured data with multiplicative smoothing and value picking regularization," *Inverse Prob.*, vol. 25, no. 2, pp. 024004–16, Feb. 2009.

[15] S. Van den Bulcke, "A 2.5D Electromagnetic Quantitative Inverse Scattering Technique to Visualize Concealed Objects Using Millimeter Waves," Ph.D. dissertation, Ghent University, Ghent, Belgium, 2010.

[16] S. Van den Bulcke, A. Franchois, and D. De Zutter, "2.5D quantitative millimeter wave imaging of a hidden object on a simplified human body model using value picking regularization," *J. Infrared Milli. Terahertz Waves*, vol. 31, pp. 1478–1490, 2010.

[17] D. Colton and P. Monk, "A modified dual space method for solving the electromagnetic inverse scattering problem for an infinite cylinder," *Inverse Prob.*, vol. 10, pp. 87–107, 1994.

[18] L. Crocco and T. Isernia, "Inverse scattering with real data: Detecting and imaging homogeneous dielectric objects," *Inverse Prob.*, vol. 17, no. 6, pp. 1573–1583, 2001.

[19] A. Abubakar and P. M. van den Berg, "The contrast source inversion method for location and shape reconstructions," *Inverse Prob.*, vol. 18, pp. 495–510, 2002.

[20] O. M. Bucci and T. Isernia, "Electromagnetic inverse scattering: Retrievable information and measurement strategies," *Radio Sci.*, vol. 32, no. 6, pp. 2123–2137, Nov.–Dec. 1997.

[21] O. Feron, B. Duchene, and A. Mohammad-Djafari, "Microwave imaging of inhomogeneous objects made of a finite number of dielectric and conductive materials from experimental data," *Inverse Prob.*, vol. 21, no. 6, pp. S95–S115, Dec. 2005.

[22] K. Belkebir and M. Saillard, "Testing inversion algorithms against experimental data: Inhomogeneous targets," *Inverse Prob.*, vol. 21, no. 6, pp. S1–S3, Dec. 2005.
[23] S. Van den Bulcke and A. Franchois, "A full-wave 2.5D volume integral equation solver for 3D millimeter-wave scattering by large inhomogeneous 2-D objects," *IEEE Trans. Antennas Propag.*, vol. 57, no. 2, pp. 535–545, Feb. 2009.
[24] R. Fletcher, *Practical Methods of Optimization*. New York, NY, USA: Wiley, 1990.
[25] A. Franchois, "Contribution à la Tomographie Microonde: Algorithmes de Reconstruction Quantitative et Vérifications Expérimentales," Ph.D. dissertation, Univ. Paris-Sud, Paris, France, 1993.
[26] M. Bertero, C. De Mol, and E. R. Pike, "Linear inverse problems with discrete data: II. Stability and regularization," *Inverse Prob.*, vol. 4, no. 2, pp. 573–594, 1988.
[27] J. M. Geffrin, P. Sabouroux, and C. Eyraud, "Free space experimental scattering database continuation: Experimental set-up and measurement precision," *Inverse Prob.*, vol. 21, no. 6, pp. S117–S130, Dec. 2005.
[28] A. Abubakar, P. M. van den Berg, and T. M. Habashy, "Application of the multiplicative regularized contrast source inversion method on TM- and TE-polarized experimental Fresnel data," *Inverse Prob.*, vol. 21, no. 6, pp. S5–S13, Dec. 2005.
[29] A. G. Tijhuis, M. C. van Beurden, and P. Zwamborn, "Iterative solution of field problems with a varying physical parameter," *Turk. J. Elec. Engin.*, vol. 10, no. 2, pp. 163–167, 2002.
[30] M. Donelli, D. Franceschini, A. Massa, M. Pastorino, and A. Zanetti, "Multi-resolution iterative inversion of real inhomogeneous targets," *Inverse Prob.*, vol. 21, no. 6, pp. S51–S63, Dec. 2005.
[31] A. Baussard, "Inversion of multi-frequency experimental data using an adaptive multiscale approach," *Inverse Prob.*, vol. 21, no. 6, pp. S5–S13, Dec. 2005.
[32] A. Dubois, K. Belkebir, and M. Saillard, "Retrieval of inhomogeneous targets from experimental frequency diversity data," *Inverse Prob.*, vol. 21, no. 6, pp. S35–S79, Dec. 2005.
[33] L. Crocco, M. D'Urso, and T. Isernia, "Testing the contrast source extended born inversion method against real data: The TM case," *Inverse Prob.*, vol. 21, no. 6, pp. S33–S50, Dec. 2005.
[34] C. Yu, L.-P. Song, and Q. H. Liu, "Inversion of multi-frequency experimental data for imaging complex objects by a DTA–CSI method," *Inverse Prob.*, vol. 21, no. 6, pp. S165–S178, Dec. 2005.
[35] P. Mojabi and J. LoVetri, "Enhancement of the Krylov subspace regularization for microwave biomedical imaging," *IEEE Trans. Med. Imag.*, vol. 28, no. 12, pp. 2015–2019, Dec. 2009.
[36] A. Abubakar, T. M. Habashy, G. Pan, and M. K. Li, "Application of the multiplicative regularized Gauss-Newton algorithm for three-dimensional microwave imaging," *IEEE Trans. Antennas Propag.*, vol. 60, no. 5, pp. 2431–2441, May 2012.

Sara Van den Bulcke was born in Ghent, Belgium, in 1982. She received the B.Sc. and M.Sc. degrees in electrical engineering from Ghent University, Ghent, Belgium, in 2005. Her M.Sc. thesis dealt with the design of a propagation model for wireless communication above a flat phantom. In September 2005, she joined the Electromagnetics Group in the Information Technology Department (INTEC) at Ghent University, where she received the Ph.D. degree in electrical engineering in 2010.

Her research, funded by a IWT doctoral fund, was focused on two-and-a-half dimensional forward and inverse electromagnetic scattering problems using millimeter waves. Currently, she is a Lecturer in electronics at KAHO Sint-Lieven, Ghent.

Ann Franchois (SM'99) received the M.S. degree in electrical engineering from the Ghent University, Ghent, Belgium, in 1988 and the DEA and Ph.D. degrees in optics and photonics from the University of Paris-Sud, Paris, France, in 1989 and 1993, respectively.

From 1994 to 1996, she was with the Research Division of Alcatel Bell Telephone in Antwerp, working on EMC and from 1996 to 1999, she was with the Joint Research Center of the Commission of the European Communities in Ispra, working on microwave sensing applications. From 1999 to 2000, she held a postdoctoral teaching-research position in the Electromagnetics Group, Faculty of Electrical Engineering at the Eindhoven University of Technology. In 2000, she joined the Department of Information Technology at the Ghent University, where she is currently a part-time Associate Professor. Her research interests include inverse scattering and imaging.

Daniël De Zutter (F'00) was born in 1953. He received the M.Sc. degree in electrical engineering in 1976 , the Ph.D. degree in 1981, and in 1984 he completed a thesis leading to a degree equivalent to the French Aggrégation or the German Habilitation, from the University of Ghent, Ghent, Belgium.

From 1976 to 1984, he was a Research and Teaching Assistant at the University of Ghent. From 1984 to 1996, he was with the National Fund for Scientific Research of Belgium. He is now a Full Professor of electromagnetics. Most of his earlier scientific work dealt with the electrodynamics of moving media. Between 2004 and 2008, he served as the Dean of the Faculty of Engineering of Ghent University and is now the Head of the Department of Information Technology. His research now focuses on all aspects of circuit and electromagnetic modelling of high-speed and high-frequency interconnections and packaging, on electromagnetic compatibility (EMC) and numerical solutions of Maxwell's equations. As author or coauthor he has contributed to more than 140 international journal papers and 150 papers in conference proceedings. In 1993, he coauthored the book *Electromagnetic and Circuit Modelling of Multiconductor Transmission Lines* in the Oxford Engineering Science Series.

Dr. De Zutter received the 1990 Montefiore Prize of the University of Liège and was corecipient of the 1995 IEEE Microwave Prize Award from the IEEE Microwave Theory and Techniques Society for "Best Publication in the Field of Microwaves" for the year 1993. In 1990, he was elected as a Member of the Electromagnetics Society. In 1999, he received the IEEE TRANSACTIONS Prize Paper Award from the IEEE EMC Society. He is an Associate Editor for the IEEE MICROWAVE THEORY AND TECHNIQUES TRANSACTIONS.